Pyrochlore electrons under pressure, heat and field: shedding light on the iridates

William Witczak-Krempa[1], Ara Go[2], Yong Baek Kim[1,3]
[1]*Department of Physics, University of Toronto, Toronto, Ontario M5S 1A7, Canada*
[2]*Department of Physics, Columbia University, New York, New York 10027, USA*
[3]*School of Physics, Korea Institute for Advanced Study, Seoul 130-722, Korea*
(Dated: October 2, 2012)

We study the finite temperature and magnetic field phase diagram of electrons on the pyrochlore lattice subject to a local repulsion as a model for the pyrochlore iridates. We provide the most general symmetry-allowed Hamiltonian, including next-nearest neighbour hopping, and relate it to a Slater-Koster based Hamiltonian for the iridates. It captures Lifshitz and/or thermal transitions between several phases such as metals, semimetals, topological insulators and Weyl semimetals, and gapped antiferromagnets with different orders. Our results on the charge conductivity, both DC and optical, Hall coefficient, magnetization and susceptibility show good agreement with recent experiments and provide new predictions. As such, our effective model sheds light on the pyrochlore iridates in a unified way.

arXiv:1208.4099v2 [cond-mat.str-el] 28 Sep 2012

The pyrochlore iridates, $R_2Ir_2O_7$ (R-227) where R is a rare earth, provide an ideal setup to study the interplay of correlations, band topology and frustration. Building in part on the strong role of spin orbit coupling (SOC) and correlations for Ir[1], various novel phases have been predicted to potentially occur in this family of complex oxides such as fractionalized topological insulators[2, 3] (TIs), chiral spin liquids[4], topological Weyl semimetals[5, 6] (TWSs), and axion insulators[5, 7]. This has contributed to a substantial experimental effort[8–21], in particular to determine the nature of the still-elusive magnetic ordering. Recent theoretical and experimental work has been pointing towards a $q = 0$ all-in/all-out (AIO) magnetic pattern in the groundstate[5, 6, 14–16, 20, 21] but direct evidence is still lacking. Another question concerns the nature of the metal insulator transition as a function of chemical pressure via the change of the R-site element[8, 11, 12] or hydrostatic pressure[17, 18], as well as the nature of the thermal continuous transitions: what are the respective roles of magnetic ordering, Mott physics, and band structure? Finally, are any of the new phases, for example the TWS, present in the actual compounds?

We provide insight into these questions by considering a microscopically-motivated Hubbard model which we probe at finite temperature and magnetic field. We compute transport, magnetization and susceptibility in the various phases (metal (M), TI, TWS, AIO, antiferromagnet (AF), etc) as well as their behaviour across the phase transitions, quantum or thermal. The similarity of our results with recent experimental data allows us to make guesses on the locations of different iridates in our phase diagram (PD), and make predictions for future experiments. Before considering the observables, we discuss a fully general Hubbard Hamiltonian on the pyrochlore lattice, its relation to previous models used for the iridates, and to the new model underlying this work.

Model demystified: The iridium ions form a pyrochlore lattice of corner-sharing tetrahedra and have a partially filled shell of 5d electrons. This results in the local repulsion and spin orbit coupling being of similar size, both on the order of 0.5-1 eV[2, 5]. The localized f-electrons of the R-site (absent for Y) can complicate the picture for some members of the iridates family for which the R-site ion carries a net magnetic moment. In this work we shall not consider the interplay between these local moments and the more itinerant Ir d-electrons. As such, our results apply directly to the compounds with Y, Lu and Eu for which this complication does not arise. Regarding the compounds with a magnetic R-site, the Ir d-electron physics might still play a key role. Indeed, the similarity of the phenomena across the pyrochlore iridates family, independent of whether the R-site is magnetic or not, provide weight to this statement[8, 9, 11–13, 21].

Rather than starting with a specific microscopic model for the iridates, we consider the most generic, time-reversal invariant Hubbard Hamiltonian on the pyrochlore lattice. We shall focus on an effective model with a single Kramers' doublet at each Ir site. This will lead to an 8-band model that we believe is sufficient to capture the salient physics. We write the Hamiltonian in a *global* basis for the pseudospin to emphasize its simplicity and generality:

$$H_0 = \sum_{\langle i,j\rangle} c_i^\dagger (t_1 + i t_2 \boldsymbol{d}_{ij}\cdot\boldsymbol{\sigma}) c_j + \sum_{\langle\langle i,j\rangle\rangle} c_i^\dagger (t_1' + i[t_2' \boldsymbol{\mathcal{R}}_{ij} + t_3' \boldsymbol{\mathcal{D}}_{ij}]\cdot\boldsymbol{\sigma}) c_j \,, \quad (1)$$

where $\boldsymbol{\sigma}$ is a vector of Pauli matrices acting on the pseudospin degree of freedom, which in the context of the iridates can be thought of as arising from the splitting of the t_{2g} levels by SOC[1] and/or trigonal distortions[22, 23] and subsequent projection onto a half-filled doublet near the Fermi level (E_F). The real vectors $\boldsymbol{d}_{ij}, \boldsymbol{\mathcal{R}}_{ij}, \boldsymbol{\mathcal{D}}_{ij}$ depend on the given bond as follows: $\boldsymbol{d}_{ij}$ is aligned along the opposite bond of the tetrahedron containing i, j; it is parallel or antiparallel with the nearest neighbor (NN)

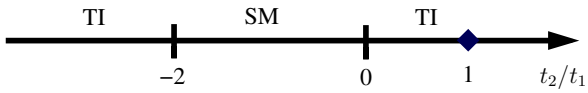

FIG. 1. PD of the generic NN hopping Hamiltonian on a pyrochlore lattice. It has two possible phases: a TI and a SM. The square indicates the presence of a gap closing, surrounded by the TI phase.

Dzyaloshinski-Morya (DM) vector of a spin model on the pyrochlore lattice, of which there are only two symmetry-allowed configurations[6, 24], differing by a global sign. $\boldsymbol{\mathcal{R}}_{ij}, \boldsymbol{\mathcal{D}}_{ij}$ are obtained by going to the next nearest neighbour (NNN) via the common NN site and taking a cross product of the two bond or $\boldsymbol{d}_{ij}$ vectors encountered, respectively. See the Supplemental Material for details regarding the construction of Eq. (1). The five real hopping amplitudes lead to a four-parameter free model, to which we add a Hubbard repulsion term, $H_U = U\sum_i (n_i - 1)^2$. In this work we perform a mean field decoupling of H_U in the magnetic channel, but expect many results to survive the inclusion of quantum many-body effects[7]. Before discussing the relation of Eq. (1) to previous microscopic models for the iridates and to the one used in this work, we briefly discuss the PD including only NN hopping. It depends on a single parameter, t_2/t_1, and can be determined exactly at half-filling; the result is shown in Fig. 1. For $-2 < t_2/t_1 < 0$ a semimetal (SM) results, and otherwise we have a TI[25], with the exception of $t_2/t_1 = 1$ where an accidental gap closing occurs. Interestingly, it does not alter the topological structure of the Hamiltonian such that the TI survives to arbitrary large values of t_2/t_1. The SM is characterized by lines of nodes between the Γ and L points. The phase transitions at $t_2/t_1 = -2, 0$ occur via gap closing/opening at the Γ point. At $t_2 = 0$, the Hamiltonian can be diagonalized analytically[26]. Interestingly, it is also the case at $t_2/t_1 = -2$, where the band structure corresponds exactly to the $t_2 = 0$ case, albeit with a spectrum inversion; specifically: $\{t_1 = 1, t_2 = -2\}$ maps to $\{-3, 0\}$. The phase transition at $t_2/t_1 = 0$ was previously discussed[27], where the $t_{1,2}$ model was identified as the most general NN symmetry-allowed Hamiltonian.

We now relate the general parameters to microscopically-motivated ones for the iridates. We first consider the case of no trigonal distortion[2, 6], leading to ideal oxygen octahedra surrounding the iridiums. The SOC splits the t_{2g} manifold into $J_{\text{eff}} = 1/2$ and 3/2 multiplets. Projecting onto the half-filled doublet near E_F yields a pseudospin $J_{\text{eff}} = 1/2$ description. Going from the atomic picture to the lattice, we introduce oxygen-mediated[2] and direct[6] overlap NN hopping t_{oxy} and t_σ, t_π, respectively. These relate to the

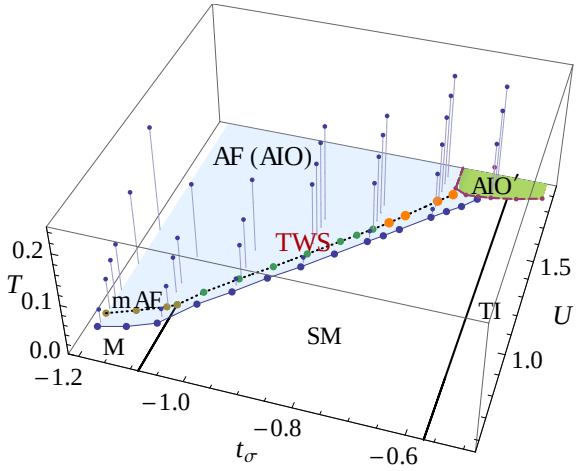

FIG. 2. Finite U & T mean field PD, including small NNN hopping ($t_{\text{oxy}} = 1$). The two shaded regions correspond to AF phases: either the AIO AF, or a type related by $\pi/2$ rotations, AIO′. The solid/dashed lines denote 2nd/1st order transitions, while the dotted lines, a gap closing signaling a Lifshitz transition out of the TWS or metallic AF (mAF).

generic model hoppings via:

$$
\begin{aligned}
t_1 &= \frac{130t_{\text{oxy}}}{243} + \frac{17t_\sigma}{324} - \frac{79t_\pi}{243}; \qquad t_1' = \frac{233t_\sigma'}{2916} - \frac{407t_\pi'}{2187};\\
t_2 &= \frac{28t_{\text{oxy}}}{243} + \frac{15t_\sigma}{243} - \frac{40t_\pi}{243}; \qquad t_2' = \frac{t_\sigma'}{1458} + \frac{220t_\pi'}{2187};\\
t_3' &= \frac{25t_\sigma'}{1458} + \frac{460t_\pi'}{2187};
\end{aligned}
\tag{2}
$$

where we have also added $t'_{\sigma,\pi}$, the σ- and π-overlap NNN hoppings. We see that the microscopic model already saturates the general Hamiltonian. As such, small trigonal distortions[22] will renormalize the $t_a^{(\prime)}$ but will not contribute new terms allowing us to use the $J_{\text{eff}} = 1/2$ description without loss of generality. We mention that Ref. 2 used purely oxygen mediated hopping, hence their large SOC TI can be mapped to $t_2/t_1 = 14/65 \approx 0.215$ which lies in the right phase as shown in Fig. 1. Also, Ref. 26 studied TIs in the t_1, t_2' model.

We shall work in units of t_{oxy} from this point. As before, we choose a representative subset of direct hoppings, $t_\pi = -2t_\sigma/3$, which translates to $t_1 = 0.53 + 0.27t_\sigma$ and $t_2 = 0.12 + 0.17t_\sigma$. We include small NNN hoppings: $t'_\sigma/t_\sigma = t'_\pi/t_\pi = 0.08$. These are expected to appear in the effective pseudospin model, and will remove line Fermi surfaces at E_F in some portions of the PD, giving instead a TWS with a Fermi surface of points or metal with small pockets[6]. The line nodes are an artifact of the NN band structure.

Finite U & T: The mean field PD is shown in Fig. 2. At $T = 0$ and small U, it contains metallic (M), SM and TI phases depending on t_σ. By M we mean a state with pockets while SM is associated with a quadratic band

touching, that splits into linear dispersing touchings in the AF TWS[6], see Fig. 3 c). The shaded regions break TRS either with the AIO order (pale), or non-collinear states which are related to the AIO state by local $\pi/2$ rotations[6] (denoted by AIO$'$). At intermediate U, there is an extended region of TWS, which turns into a metallic AF (mAF) for $t_\sigma < -1.085$. The latter is actually a tilted TWS, where the 3D "Dirac cones" have been tilted such as to create metallic pockets, but with the "Weyl touchings" remaining. These phases should be compared with similar results obtained in Ref. [6] by two of us. The main difference is that we have now included the NNN hoppings in the self-consistent calculation. Indeed, the previous work was mainly concerned with the self-consistent analysis of the NN Hamiltonian: the NNN hoppings were added to the final spectrum to establish that the line-nodes at E_F can give rise to a Weyl phase when the ordering is of the AIO type. The present work confirms this. Moreover, a metallic phase now appears for $t_\sigma < -1.085$, which will be relevant when we compare with experiments on the iridates. Another new feature is the presence of magnetization jumps that appear within the AIO phase, present for $-0.78 < t_\sigma < -0.68$, denoted by the orange (larger) markers in Fig. 2. The spontaneous onsite magnetization, m, grows discontinuously along that line and the TWS becomes a gapped AF insulator: energetically, the system finds it preferable to preempt the continuous annihilation of Weyl points of opposite chirality via a discontinuous evolution of m. The jumps, or else the abrupt continuous increase for $t_\sigma < -0.78$, seem tied to the peculiar spectrum of the TWS.

Turning to finite temperature, we find that most thermal transitions are continuous; this is denoted by the out-of-plane fibers ended by circular markers in Fig. 2. We have also examined the model at larger NNN hoppings, $t'_{\sigma,\pi}/t_{\sigma,\pi} = 0.16$, and found that small regions of 1st order transitions to the AIO phase appear at intermediate U. As can be seen in Fig. 2, the transition temperatures naturally increase with U, since an increase in the latter leads to larger gaps. Thus, *the gapless TWS is fairly unstable to melting at finite* T, with typical transition temperatures $T_c \sim 0.01$.

Optical conductivity: We examine the optical conductivity associated with the various phases, as illustrated in Fig. 3. Panel a) shows the Lifshitz transition associated with a change in the Fermi surface topology from a metal with small electron- and hole-like pockets at $U = 0$ to a gapped AIO state at $U = 1$. The optical conductivity in panel b) reflects this via a small Drude peak in the former case, and a gap in the latter. Panel c) shows the spectra of the TWS and quadratic band touching SM out of which it arose. The associated conductivities are reduced approaching the DC limit because these two states have a vanishing density of states (DOS) at E_F. We note the distinguishing peak at low frequency for the TWS: it

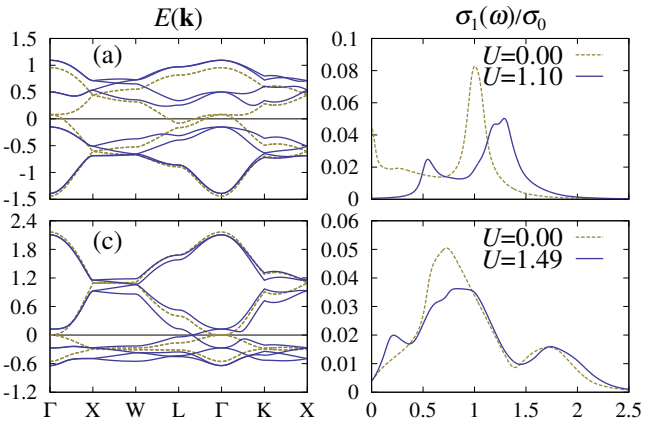

FIG. 3. Spectra and corresponding optical conductivity for $t_\sigma = -1.2$, a) & b), and $t_\sigma = -0.8$, c) & d). Panel a) shows the spectrum ($E_F = 0$) for the M and AIO insulator, while b) for the SM and TWS. The conductivity is in units of $\sigma_0 = e^2/\hbar a_0 \sim 10^4\,(\Omega\cdot\mathrm{cm})^{-1}$, where $a_0 = a/4$ and $a \approx 1.0$ nm is the FCC lattice constant.

receives weight from transitions across the depleted energy range corresponding to the TWS, where the DOS vanishes quadratically.

DC transport: We turn to the DC electric transport, which provides further insight into the PD. The AIO state has isotropic conductivities due to the highly symmetric magnetic configuration, i.e. $\sigma_{xx} = \sigma_{yy} = \sigma_{zz}$. The same holds for the Hall conductivities: $\sigma_{xy} = \sigma_{yz} = \sigma_{zx}$. This will cease to be true for the AIO$'$ states, which select a given direction[6]. To compute the transport coefficients in the DC limit, we introduce a momentum independent scattering time, τ. For example, the longitudinal conductivity is given by[28, 29]

$$\sigma_{xx} = e^2\tau\frac{1}{V}\sum_{\boldsymbol{k},\alpha}\left(-\frac{\partial n_F}{\partial\epsilon_\alpha(\boldsymbol{k})}\right)\left(v_x^\alpha(\boldsymbol{k})\right)^2, \qquad (3)$$

where $1 \le \alpha \le 8$ is the band index and $\boldsymbol{v}^\alpha = \partial_{\boldsymbol{k}}\epsilon_\alpha$. Fig. 4 shows the longitudinal resistivity, ρ_{xx}, and Hall coefficient, R_H, at $t_\sigma = -1.2$ and $U = 1.25$ as a function of temperature. At large temperatures, the system is in a paramagnetic metallic state, with the expected $d\rho_{xx}/dT > 0$. As T is lowered beneath $T_c = 0.21$, the system undergoes a continuous transition to the AIO AF: the on-site magnetization increases resulting in the spectrum evolving from being gapless at T just below T_c, to a fully gapped AF. We indeed find that the resistivity shows a rapid upturn at T_c (where the slope changes sign) and becomes exponentially activated at low T. The Hall coefficient also shows a signature at the transition. Note that the latter is positive suggesting hole-like carriers in that portion of the phase diagram. The behaviour of the resistivity and sign of the Hall coefficient are consistent with recent experiments on Eu-227[11, 12, 15, 17].

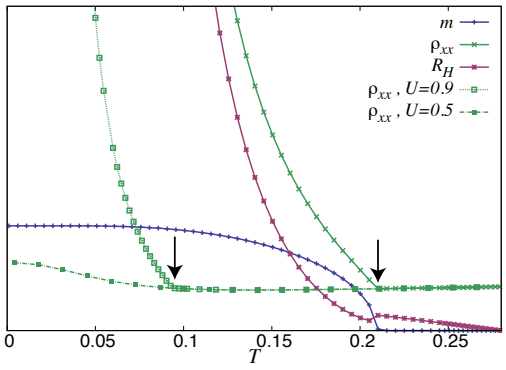

FIG. 4. Solid lines: on-site magnetization (m), DC resistivity (ρ_{xx}) and Hall coefficient (R_H) for $t_\sigma = -1.2$ and $U = 1.25$. The non-solid lines show ρ_{xx} for $U = 0.9$ and 0.5. The arrows indicate the locations of the continuous transitions, at which ρ_{xx} shows a rapid upturn. The vertical axis goes from zero to positive values in arbitrary units.

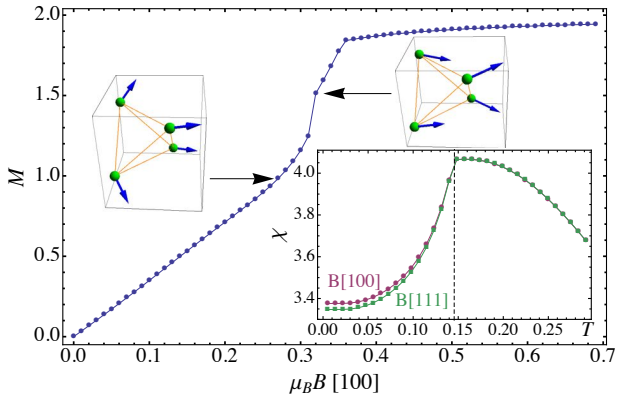

FIG. 5. Main: magnetization per unit cell, M, as a function of an applied magnetic field along the [100] direction for the AIO insulator at $t_\sigma = -1.2$ and $U = 2.1$. The evolution of the magnetic moments across an abrupt feature is shown. Inset: Susceptibility for fields along [100] and [111] versus T. The dashed line corresponds to the 2nd order transition.

Fig. 4 also shows the evolution of the resistivity as the ratio of the Hubbard repulsion to the bandwidth is reduced. The transition occurs at a lower temperature at $U = 0.9$ compared to 1.25, as is expected because the onsite magnetization is reduced and the corresponding groundstate has a smaller gap. At sufficiently small U, the system does not develop magnetic ordering and the $T = 0$ metallic bandstructure is present at all temperatures, in particular this leads to a finite $T = 0$ resistivity. This behaviour resembles what happens in the iridates as the size of the R-site ion is increased[8, 11, 12] (chemical pressure). It also roughly agrees with hydrostatic pressure experiments on Eu-227[17] with the difference that T_c was not found to change appreciably with pressure, unlike for Nd-227[18].

Magnetic field: We examine the effects of a magnetic field on the various ground states of Fig. 2 via the addition of a Zeeman coupling to the Hubbard Hamiltonian. We have considered fields along the [100], [110] and [111] directions. In all cases, we find a rather continuous evolution to a fully polarized paramagnetic state, without any first order transition to a FM aligned with the field, in contrast with Ref. 5. Instead, the net magnetization grows until it (asymptotically) reaches a fully polarized state, as shown in Fig. 5. The magnetization profiles present small features that correspond to sudden changes in the magnetic order (never to a FM, though), but lead to small changes in the actual magnetization. One such abrupt evolution is seen to occur around $\mu_B B \approx 0.32$ in Fig. 5. The susceptibility, χ, as a function of temperature is shown in the inset of Fig. 5 for fields along [100] and [111]; with $\chi[110] = \chi[100]$. For $T > T_c = 0.148$, χ is isotropic and slowly varying. As T is lowered, χ has a maximum at T_c, beyond which point it becomes slightly anisotropic. We find that in the ordered phase, $\chi[100] > \chi[111]$. All of these features are consistent with recent measurements of the zero-field cooled (ZFC) susceptibility of Eu-227[15].

Discussion: Our PD, Fig. 2, and results for the transport and magnetic properties at finite T and field suggest that our new model is apt to describe many salient features of the pyrochlore iridates family. In particular, in light of recent experiments[11, 15, 17] that show the presence of a charge gap in Eu-227, we suggest that its ground state is an AIO gapped insulator, which under pressure can undergo a Lifshitz transition to a non-magnetic metal with small pockets, although TWS and metallic AF (with coexisting Weyl nodes and pockets) are possible. At sufficiently high temperatures, we find that the magnetic order melts continuously leading to a paramagnetic metal, consistent with experiments. For Y-227, which shows insulating behaviour at all temperatures ($d\rho/dT < 0$), we suggest that the high temperature non-magnetic state (connected to the $U = 0$ parent phase) is a semimetal. Finally, the TWS, which melts at very low temperatures, is probably not present in the ground states of Eu- and Y-227 because of the evidence for a finite gap but it might be accessible by hydrostatic[17, 18], or chemical pressure as was suggested for Nd-227[20].

We thank D. Drew and A. Sushkov for sharing preliminary optical conductivity data with us. We acknowledge helpful discussions with L. Balents, S. Bhattacharjee, S. R. Julian, A.J. Millis, S. Nakatsuji, J. Rau, and F. F. Tafti. This work was supported by NSERC, CIFAR, the Center for Quantum Materials at the University of Toronto (WWK,YBK), a Walter Sumner fellowship (WWK), and by the US Department of Energy under grant DOE FG02-04ER46169 (AG). Some part of this work was done at the Aspen Center for Physics, partially funded by NSF Grant #1066293.

Constructing the general Hamiltonian

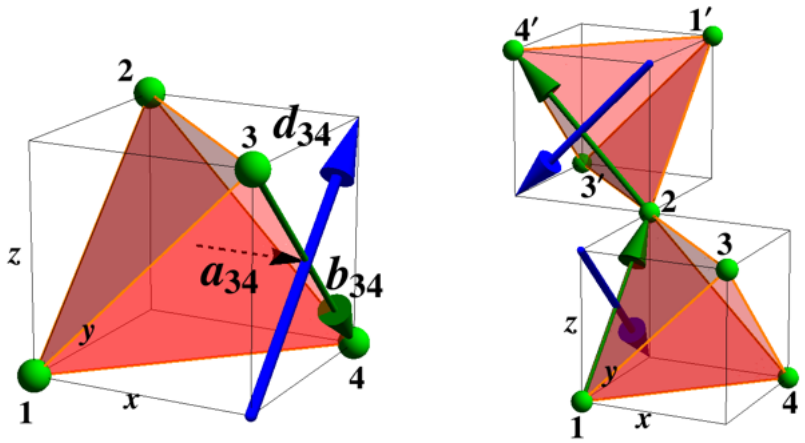

(a) (b)

FIG. 6. Definitions of vectors entering into the general Hamiltonian. The green (thin) arrows correspond to the $\boldsymbol{b}_{ij}$, whereas the blue (thick) ones to the $\boldsymbol{d}_{ij}$. b) shows the vectors involved in obtaining the NNN hopping amplitude between sites 1 and $4'$, who share a common NN, site 2.

We provide details regarding the construction of the Hamiltonian used in the main text. We choose the basis vectors of the pyrochlore lattice to be Fig. 6 a): $\boldsymbol{b}_1 = (0,0,0)\,, \boldsymbol{b}_2 = (0,1,1)\,, \boldsymbol{b}_3 = (1,0,1)\,, \boldsymbol{b}_4 = (1,1,0)$. In these units the FCC unit cell has dimension $a = 4$. As stated in the main text, the most general hopping Hamiltonian on the pyrochlore lattice takes the form:

$$H_0 = \sum_{\langle i,j\rangle} c_i^\dagger (t_1 + it_2 \boldsymbol{d}_{ij}\cdot\boldsymbol{\sigma}) c_j + \sum_{\langle\langle i,j\rangle\rangle} c_i^\dagger (t_1' + i[t_2' \boldsymbol{\mathcal{R}}_{ij} + t_3' \boldsymbol{\mathcal{D}}_{ij}]\cdot\boldsymbol{\sigma}) c_j \,, \tag{4}$$

where the NN Hamiltonian is built using the vectors:

$$\boldsymbol{d}_{ij} = 2\boldsymbol{a}_{ij} \times \boldsymbol{b}_{ij}\,, \tag{5}$$

$$\boldsymbol{a}_{ij} = \frac{1}{2}(\boldsymbol{b}_i + \boldsymbol{b}_j) - \boldsymbol{x}_c\,, \tag{6}$$

$$\boldsymbol{b}_{ij} = \boldsymbol{b}_j - \boldsymbol{b}_i\,, \tag{7}$$

where it is understood in these definitions that $\boldsymbol{b}_i$ selects the basis vector of the full lattice (Bravais + basis) index, i. $\boldsymbol{a}_{ij}$ points from the center of the tetrahedron, $\boldsymbol{x}_c = (1,1,1)/2$, to the middle of the $\langle i,j\rangle$ bond; it is always orthogonal to the faces of the cube built out of the tetrahedron's vertices, see Fig. 6. $\boldsymbol{b}_{ij}$ is the NN bond vector pointing from site i to site j. We have chosen the notation for the $\boldsymbol{d}_{ij}$ in analogy with the Dzyaloshinski-Morya (DM) vectors, $\boldsymbol{D}_{ij}$, of a spin model on the pyrochlore lattice because both sets of vectors are parallel or antiparallel on all bonds. The difference arises in the sign. There are only two symmetry-allowed configurations of DM vectors[6, 24], differing by a global sign. The $\boldsymbol{d}_{ij}$'s are always found to differ by a sign on some bonds with either type of DM vectors.

The NNN Hamiltonian simply uses cross products of the $\boldsymbol{b}_{ij}$'s and $\boldsymbol{d}_{ij}$'s:

$$\boldsymbol{\mathcal{R}}_{ij} = \boldsymbol{b}_{ik} \times \boldsymbol{b}_{kj}\,, \tag{8}$$

$$\boldsymbol{\mathcal{D}}_{ij} = \boldsymbol{d}_{ik} \times \boldsymbol{d}_{kj}\,, \tag{9}$$

where i and j are NNNs and share the site k as their (unique) common NN. $\boldsymbol{\mathcal{R}}_{ij}, \boldsymbol{\mathcal{D}}_{ij}$ are obtained by going to the NNN via the common NN site and taking a cross product of the two bond or $\boldsymbol{d}$ vectors encountered, respectively. Fig. 6 b) illustrates the vectors necessary to construct the NNN amplitude between sites 1 and $4'$. We note that $\boldsymbol{\mathcal{R}}_{ij}$ and $\boldsymbol{\mathcal{D}}_{ij}$ always point along the diagonals (s_1, s_2, s_3), where $s_i = \pm 1$. For instance, $\boldsymbol{\mathcal{R}}_{34} = (1,-1,1)$ and $\boldsymbol{\mathcal{D}}_{34} = (-1,1,1)$, as can be read off from Fig. 6; they are linearly independent as it should. For completeness, we

provide the momentum-space form of the Hamiltonian, $H = \sum_{\boldsymbol{q}} c_a^\dagger(\boldsymbol{q})(\mathcal{H}_{ab}^{\rm NN}(\boldsymbol{q}) + \mathcal{H}_{ab}^{\rm NNN}(\boldsymbol{q}))c_b(\boldsymbol{q})$, with

$$\mathcal{H}_{ab}^{\rm NN}(\boldsymbol{q}) = 2(t_1 + t_2 i\boldsymbol{\sigma}\cdot\boldsymbol{d}_{ab})\cos\left[\boldsymbol{q}\cdot\boldsymbol{b}_{ab}\right] , \tag{10}$$

$$\mathcal{H}_{ab}^{\rm NNN}(\boldsymbol{q}) = 2\sum_{c\neq a,b}\{t_1'(1-\delta_{ab}) + i\boldsymbol{\sigma}\cdot[t_2'(\boldsymbol{b}_{ac}\times\boldsymbol{b}_{cb}) + t_3'(\boldsymbol{d}_{ac}\times\boldsymbol{d}_{cb})]\}\cos\left[\boldsymbol{q}\cdot(-\boldsymbol{b}_{ac}+\boldsymbol{b}_{cb})\right] , \tag{11}$$

where the indices $1 \leq a, b, c \leq 4$ run over the basis sites. The sum over c in the NNN Hamiltonian runs over the choice of common NN between NNNs on sublattices a and b. There are two such sites: $c \in \{1,2,3,4\} \setminus \{a,b\}$.

Ref. 26 discussed the t_1, t_2' model, with a special focus on topological insulator phases. Ref. 27 identified the t_1, t_2 model as the most general NN, time-reversal-invariant hopping Hamiltonian on the pyrochlore lattice, for a single (pseudo)spin-1/2 Hilbert space per site. (We note that these two works use $\boldsymbol{d}_{ij}$ to denote our $\boldsymbol{b}_{ij}$.)

Relation to microscopically motivated Hamiltonian

Two of us have previously proposed a model for the pyrochlore iridates, which was mainly analysed at the NN level[6]. It extends a previous one[2], to which we added hopping amplitudes arising from the direct overlaps of the d-orbitals of Ir. These Slater-Koster like models are more naturally expressed in a local basis because of the relative rotations between the oxygen octahedra within a unit cell, an illustration of this is found in Ref. 6. It is however useful to consider the same Hamiltonians expressed in a global basis instead, to see the role of the different microscopic hoppings more clearly.

We have taken the microscopic, local-axis Hamiltonian given by Eq. (1) in Ref. 6, supplemented by NNN direct hoppings, and have performed spinor rotations to obtain a Hamiltonian in a global basis for the pseudospin. This was compared with Eq. (4) to obtain the relation between $\{t_1, t_2, t_1', t_2', t_3'\}$ and $\{t_{\rm oxy}, t_\sigma, t_\pi, t_\sigma', t_\pi', t_\delta'\}$, as given in the main text. Compared with the main body, we in addition include the NNN hopping arising from the δ-overlap, t_δ', leading to:

$$\begin{aligned}
t_1 &= \frac{130t_{\rm oxy}}{243} + \frac{17t_\sigma}{324} - \frac{79t_\pi}{243}; \qquad t_1' = \frac{233t_\sigma'}{2916} - \frac{407t_\pi'}{2187} - \frac{1843t_\delta'}{8748};\\
t_2 &= \frac{28t_{\rm oxy}}{243} + \frac{15t_\sigma}{243} - \frac{40t_\pi}{243}; \qquad t_2' = \frac{t_\sigma'}{1458} + \frac{220t_\pi'}{2187} + \frac{277t_\delta'}{4374};\\
t_3' &= \frac{25t_\sigma'}{1458} + \frac{460t_\pi'}{2187} - \frac{275t_\delta'}{4374};
\end{aligned} \tag{12}$$

The NNN hopping t_δ' was added in order to have a number of degrees of freedom matching that of the general Hamiltonian at the NNN level. One can also consider the NNN oxygen-mediated hopping, which will add an analogous term to the t_i'.

[1] B. J. Kim, H. Jin, S. J. Moon, J.-Y. Kim, B.-G. Park, C. S. Leem, J. Yu, T. W. Noh, C. Kim, S.-J. Oh, J.-H. Park, V. Durairaj, G. Cao, and E. Rotenberg, Phys. Rev. Lett. **101**, 076402 (2008); B. J. Kim, H. Ohsumi, T. Komesu, S. Sakai, T. Morita, H. Takagi, and T. Arima, Science **323**, 1329 (2009).
[2] D. Pesin and L. Balents, Nat Phys **6**, 376 (2010).
[3] W. Witczak-Krempa, T. P. Choy, and Y. B. Kim, Phys. Rev. B **82**, 165122 (2010).
[4] Y. Machida, S. Nakatsuji, S. Onoda, T. Tayama, and T. Sakakibara, Nature **463**, 210 (2009).
[5] X. Wan, A. M. Turner, A. Vishwanath, and S. Y. Savrasov, Phys. Rev. B **83**, 205101 (2011).
[6] W. Witczak-Krempa and Y. B. Kim, Phys. Rev. B **85**, 045124 (2012).
[7] A. Go, W. Witczak-Krempa, G. S. Jeon, K. Park, and Y. B. Kim, "Correlated topological phases in 3D complex oxides via Green's functions," (PRL, in press), arXiv:1202.4460.
[8] D. Yanagishima and Y. Maeno, Journal of the Physical Society of Japan **70**, 2880 (2001).
[9] N. Taira, M. Wakeshima, and Y. Hinatsu, Journal of Physics: Condensed Matter **13**, 5527+ (2001).
[10] H. Fukazawa and Y. Maeno, Journal of the Physical Society of Japan **71**, 2578 (2002).
[11] K. Matsuhira, M. Wakeshima, R. Nakanishi, T. Yamada, A. Nakamura, W. Kawano, S. Takagi, and Y. Hinatsu, Journal of the Physical Society of Japan **76**, 043706+ (2007).
[12] K. Matsuhira, M. Wakeshima, Y. Hinatsu, and S. Takagi, Journal of the Physical Society of Japan **80**, 094701 (2011).

[13] T. Hasegawa, N. Ogita, K. Matsuhira, S. Takagi, M. Wakeshima, Y. Hinatsu, and M. Udagawa, Journal of Physics: Conference Series **200**, 012054+ (2010).
[14] S. Zhao, J. M. Mackie, D. E. MacLaughlin, O. O. Bernal, J. J. Ishikawa, Y. Ohta, and S. Nakatsuji, Phys. Rev. B **83**, 180402 (2011).
[15] J. J. Ishikawa, E. C. T. O'Farrell, and S. Nakatsuji, Phys. Rev. B **85**, 245109 (2012).
[16] K. Tomiyasu, K. Matsuhira, K. Iwasa, M. Watahiki, S. Takagi, M. Wakeshima, Y. Hinatsu, M. Yokoyama, K. Ohoyama, and K. Yamada, Journal of the Physical Society of Japan **81**, 034709+ (2012).
[17] F. F. Tafti, J. J. Ishikawa, A. McCollam, S. Nakatsuji, and S. R. Julian, Phys. Rev. B **85**, 205104 (2012).
[18] M. Sakata, T. Kagayama, K. Shimizu, K. Matsuhira, S. Takagi, M. Wakeshima, and Y. Hinatsu, Phys. Rev. B **83**, 041102 (2011).
[19] M. C. Shapiro, S. C. Riggs, M. B. Stone, C. R. de la Cruz, S. Chi, A. A. Podlesnyak, and I. R. Fisher, Phys. Rev. B **85**, 214434 (2012).
[20] S. M. Disseler, C. Dhital, T. C. Hogan, A. Amato, S. R. Giblin, C. de la Cruz, A. Daoud-Aladine, S. D. Wilson, and M. J. Graf, Phys. Rev. B **85**, 174441 (2012).
[21] S. M. Disseler, C. Dhital, A. Amato, S. R. Giblin, C. de la Cruz, S. D. Wilson, and M. J. Graf, Phys. Rev. B **86**, 014428 (2012).
[22] B.-J. Yang and Y. B. Kim, Phys. Rev. B **82**, 085111 (2010).
[23] M. Kargarian, J. Wen, and G. A. Fiete, Phys. Rev. B **83**, 165112 (2011).
[24] M. Elhajal, B. Canals, R. Sunyer, and C. Lacroix, Phys. Rev. B **71**, 094420 (2005).
[25] J. E. Moore and L. Balents, Phys. Rev. B **75**, 121306 (2007); R. Roy, Phys. Rev. B **79**, 195322 (2009); L. Fu, C. L. Kane, and E. J. Mele, Phys. Rev. Lett. **98**, 106803 (2007).
[26] H.-M. Guo and M. Franz, Phys. Rev. Lett. **103**, 206805 (2009).
[27] M. Kurita, Y. Yamaji, and M. Imada, Journal of the Physical Society of Japan **80**, 044708+ (2011).
[28] N. P. Ong, Phys. Rev. B **43**, 193 (1991).
[29] D. Podolsky and Y. B. Kim, Phys. Rev. B **83**, 054401 (2011).